


 Cite this: *RSC Adv.*, 2026, 16, 4575

# Influence of dextrose monohydrate on the optical properties and adsorption activity of $\text{Ni}_{0.6}\text{Zn}_{0.2}\text{Sb}_{0.2}\text{Fe}_2\text{O}_4$ nanoferrites: towards multifunctional applications

 Nourhan Mohamed Gaber,<sup>a</sup> Leen W. El Khatib,<sup>b</sup> Amani Aridi,<sup>c</sup> Alaa M. Abdallah,<sup>d</sup> Gehan M. El-Subruiti,<sup>e</sup> Mirna Omar,<sup>ef</sup> Sarah Omar<sup>ef</sup> and Ramadan Awad<sup>gh</sup>

Dyes are noxious substances that are frequently found in industrial effluent. Metal ferrites are magnetic nano-adsorbents and may be affordable and effective in removing pollutants. Capping these nanoparticles increases their stability and prevents them from aggregating. In this investigation,  $\text{Ni}_{0.6}\text{Zn}_{0.2}\text{Sb}_{0.2}\text{Fe}_2\text{O}_4$  ( $\text{Ni}_{0.6}\text{Zn}_{0.2}\text{Sb}_{0.2}\text{F}$ ) nanoparticles were capped with different concentrations of dextrose monohydrate (*D*), forming  $\text{Ni}_{0.6}\text{Zn}_{0.2}\text{Sb}_{0.2}\text{FD}$  via the co-precipitation method. The optical properties of the samples were investigated by utilizing UV-vis spectroscopy and photoluminescence spectroscopy (PL) to unveil their multifunctional potential. Several parameters were calculated, such as the band gap energy, which varied between 2.71 eV and 3.05 eV. Furthermore, the interstitial defects and the recombination process of electrons were also determined using PL. The adsorption activity of the synthesized  $\text{Ni}_{0.6}\text{Zn}_{0.2}\text{Sb}_{0.2}\text{FD}$  was investigated against the removal of methyl violet (MV). The best removal efficiency was achieved by  $\text{Ni}_{0.6}\text{Zn}_{0.2}\text{Sb}_{0.2}\text{FD}_{10}$  with a value of 78.5%, and maximum adsorption capacity ( $q_{\text{max}}$ ),  $q_{\text{max}} = 75.5 \text{ mg g}^{-1}$ . This was attained by studying several parameters, including adsorbent dosage, MV concentration, pH, temperature, and time. The optimum experimental conditions were obtained at 10 ppm MV, pH = 7, and temperature 25 °C. The adsorption process was found to follow a pseudo-second-order model, and the experimental data fit well with the Temkin non-linear isotherm models.

 Received 31st October 2025  
 Accepted 15th January 2026

DOI: 10.1039/d5ra08391e

[rsc.li/rsc-advances](http://rsc.li/rsc-advances)

## 1. Introduction

Water supplies are under threat owing to over-exploitation by humans and pollution from industrial waste and agricultural runoff. Dyes, petrochemicals, heavy metals, and pharmaceutical effluents permeate the hydrosphere annually, causing various environmental impacts. According to research, dyes enter the environment at a rate of 70 000 to 2 00 000 tons per year.<sup>1</sup> They are classified based on their chemical structure and application

technique. Methyl violet (MV) is a triphenylmethane dye, having three aryl groups attached to a nitrogen atom and one or two methyl groups with a long half-life, resulting in its vivid coloration. Furthermore, MV is a basic dye due to the positive charge on its amino groups and is composed of tetramethyl, pentamethyl, and hexamethyl pararosaniline chlorides.<sup>2</sup> This latter molecule, commonly known as crystal violet or MV10B, is the principal representative of the three dyes. In contrast, the pentamethylated molecule dominates in MV2B. The color of MV varies based on the ratio of each component.<sup>3</sup> MV is often utilized in several sectors, including paper, textile, printing, and leather, despite its carcinogenicity, non-biodegradability, toxicity, and mutagenicity.<sup>4</sup> Its bio-resistant existence in water causes turbidity and reduced light penetration, inhibiting the photosynthetic processes of aquatic plants.<sup>5</sup> Moreover, this MV discharge can impair human health by negatively impacting the respiratory system, digestive system, and kidneys. Also, it causes other symptoms, including hypertension, jaundice, accelerated heartbeat, vomiting, cyanosis, ocular discomfort, and shock.<sup>4</sup>

Removing synthetic dyes from industrial effluent is problematic due to their complicated aromatic structure and lack of

<sup>a</sup>Department of Medical Laboratories, Faculty of Applied Health Science Technology, Pharos University in Alexandria, Canal El Mahmoudia Street, Beside Green Plaza Complex, Alexandria, 21648, Egypt. E-mail: [nourhan.gaber@pua.edu.eg](mailto:nourhan.gaber@pua.edu.eg)

<sup>b</sup>Department of Chemistry, Faculty of Science, Beirut Arab University, Beirut, Lebanon

<sup>c</sup>Public Health Department, Faculty of Health Sciences, Modern University for Business and Science, Beirut, Lebanon

<sup>d</sup>Physics Department, Faculty of Science, Beirut Arab University, Beirut, Lebanon

<sup>e</sup>Chemistry Department, Faculty of Science, Alexandria University, Alexandria, Egypt

<sup>f</sup>Department of Mechanical Engineering, Universiti Teknologi PETRONAS (UTP), 32610 Bandar Seri Iskandar, Perak Darul Ridzuan, Malaysia

<sup>g</sup>Physics Department, Faculty of Science, Alexandria University, Alexandria, Egypt

<sup>h</sup>Department of Basic Sciences, Faculty of Computer Science and Artificial Intelligence, Pharos University in Alexandria, Alexandria, Egypt



biodegradability. Implementing proper techniques to eliminate MV from dye effluent is crucial for maintaining water quality and protecting human health. Several sanitation treatment technologies are often used to remove dyes from wastewater, such as physical, physicochemical, and chemical methods. These methods include membrane separation, sedimentation, coagulation, flocculation, adsorption, solvent extraction, photocatalytic oxidation, Fenton oxidation, and electrochemical approaches. Moreover, biological approaches include aerobic and anaerobic microbial decomposition, as well as the application of enzymes. Chemical and biological procedures are effective in removing hues, but they require specific tools and are energy-intensive. Additionally, they typically create significant amounts of byproducts.<sup>6</sup> The physical pollutant removal approach is green and effective as it removes the pollutants without generating by-products. Adsorption offers merits over other techniques owing to its easy implementation, simple design, significant regeneration potential, diversified material sources, strong performance, and affordability. This method is ideal for treating polluted waters as it does not need prior treatment.<sup>7</sup>

Spinel ferrite (SFs) nanoparticles are metallic oxides, defined by the generic chemical formula  $AB_2O_4$ , where the metal cations denoted by A and B are located at tetrahedral and octahedral sites, respectively. The anionic oxygen in  $AB_2O_4$  creates dense face-centered cubic (FCC) packing. Spinel ferrites have gained popularity due to their high adsorption capacity, unique magnetic and electrical characteristics, and large surface area-to-volume ratio, making them a popular choice for wastewater treatment.<sup>8</sup> According to the cations' distribution in the spinel lattice, SFs can be further categorized into three groups based on the cation distribution: normal, inverse, and mixed spinel ferrites. In normal spinel ferrites, the divalent ions are present in the tetrahedral site, while the trivalent ions are present in the octahedral site as  $ZnFe_2O_4$ . Whereas, in inverse spinel ferrites, the divalent ions are present in the octahedral site, while the trivalent ions are distributed equally between the tetrahedral and the octahedral sites as  $NiFe_2O_4$ . In mixed spinel ferrites, the divalent and trivalent ions are both present in the tetrahedral and octahedral sites, such as  $NiZnFe_2O_4$ . The mixed spinel structure has significant properties combined from both normal and inverse ones, such as high electrical resistivity, high magnetic permeability, high saturation magnetization, high corrosion resistance, low dielectric constant, and low magnetic coercivity.<sup>9</sup>

Despite the superior magnetic behaviour of SFs, agglomeration occurs between their particles, causing a lowering in active adsorption sites; thus, capping agents are used such as polysaccharides, polymers, amino acids, proteins, dendrimers, cyclodextrins, organic ligands, surfactants, and bio-extracts.<sup>10,11</sup> One of the most used capping agents is the dextrose monohydrate (*D*). *D* is a carbohydrate derivative, specifically a monosaccharide characterized by its availability, solubility in water, and low price.<sup>12</sup> The amphiphilic *D* molecules, which have polar and nonpolar heads, react with metals of SFs and with the surrounding environment, respectively. By forming covalent

bonds with the SFs, *D* causes steric hindrance, resulting in increased stability in the adsorbent.<sup>13</sup>

Previously, Khatib *et al.*<sup>12</sup> fabricated an eco-friendly uncapped and capped  $Ni_{0.6}Zn_{0.2}Sb_{0.2}FD$  relying on the characteristics of dextrose monohydrate at different concentrations. The physical and magnetic properties of the synthesized samples were published in a previous work, including the XRD, TEM, EDX, and VSM characterizations. Since the fabricated nanoferrites have the potential to be applied in dye removal, this study was performed to investigate the optical properties of the uncapped and capped  $Ni_{0.6}Zn_{0.2}Sb_{0.2}FD$  using UV-vis and PL spectroscopies. Besides, the adsorption activity of these samples was tested. A full elimination study was conducted to establish the best conditions for MV removal, such as the effect of pH, initial MV concentrations, adsorbent dosage, and the effect of temperature. The proposed adsorption pathway was predicted through a comparison between FTIR spectra before and after MV removal. Moreover, kinetics, isotherms, and thermodynamic adsorption studies were employed. Eventually, a reusability test was held to assess the stability of the capped  $Ni_{0.6}Zn_{0.2}Sb_{0.2}FD$ .

## 2. Materials and methods

### 2.1. Chemicals and materials

Iron(III) chloride hexahydrate ( $FeCl_3 \cdot 6H_2O \geq 99\%$ , honeywell Fluka), nickel(II) chloride hexahydrate ( $NiCl_2 \cdot 6H_2O \geq 98\%$ , Sigma Aldrich), zinc chloride ( $ZnCl_2 \geq 98\%$ , Sigma Aldrich), antimony(III) chloride ( $SbCl_3 \geq 99\%$ , Sigma Aldrich), sodium hydroxide pellet ( $NaOH \geq 99\%$ , Chem-Lab) and dextrose monohydrate ( $C_6H_{12}O_6 \cdot H_2O$ , Alpha Chemika). The solvents used throughout the synthesis process are deionized water and ethanol. All chemicals used were analytical grade and did not require additional purification. Furthermore, deionized water was used throughout the experiment.

### 2.2. Preparation of uncapped and capped $Ni_{0.6}Zn_{0.2}Sb_{0.2}FD$

The co-precipitation method was adopted to synthesize uncapped and capped  $Ni_{0.6}Zn_{0.2}Sb_{0.2}FD$  with different concentrations of *D*. A 1 M solution of each nickel-, zinc-, and antimony chloride was prepared separately by dissolving in deionized water under stirring to ensure full dissolving, then mixed. This was followed by the progressive addition of different concentrations of dextrose monohydrate (0 M, 0.05 M, 0.1 M, 0.2 M, and 0.35 M) dropwise to the mixtures. The final mixtures were stirred for 30 minutes, followed by titration with 3 M NaOH to adjust the pH value to 12. After that, the mixtures were heated under continuous stirring for 2 hours at 80 °C. The mixtures were then washed with a mixture of 75% deionized water and 25% ethanol to adjust the pH value to 7. Furthermore, the obtained samples were dried in an oven for 16 hours at 100 °C, ground into powder, and then calcined for 2 hours at 750 °C. The samples will be named as follows:  $Ni_{0.6}Zn_{0.2}Sb_{0.2}FD_0$ ,  $Ni_{0.6}Zn_{0.2}Sb_{0.2}FD_5$ ,  $Ni_{0.6}Zn_{0.2}Sb_{0.2}FD_{10}$ ,  $Ni_{0.6}Zn_{0.2}Sb_{0.2}FD_{20}$ , and  $Ni_{0.6}Zn_{0.2}Sb_{0.2}FD_{35}$  for *D* concentrations of 0, 0.05, 0.1, 0.2, and 0.35 M, respectively.



### 2.3. Optical studies

Optical studies were carried out by a UV-vis Jasco V-670 spectrophotometer in the range 250–700 nm. The Jasco FP-8600 spectrofluorometer was utilized to investigate the photoluminescence spectroscopy (PL) studies. In these characterization techniques, 4 mg of the uncapped and capped  $\text{Ni}_{0.6}\text{Zn}_{0.2}\text{Sb}_{0.2}\text{FD}$  were dissolved in 40 mL of HCl (2 M) and sonicated for 15 minutes. Then, the measurement was done by transforming 5 mL of the solution into a quartz cuvette.

### 2.4. Adsorption studies

The MV dye adsorption experiments were performed in batch mode. Different amounts of  $\text{Ni}_{0.6}\text{Zn}_{0.2}\text{Sb}_{0.2}\text{FD}_{10}$  (0.01–0.04 g) were added to 20 mL solutions of MV dye with initial concentrations ranging from 10 to 50  $\text{mg L}^{-1}$ . The pH of the solution was adjusted between 3 and 11 using 0.1 M HCl and 0.1 M NaOH solutions, and the temperature during adsorption varied from 25 to 55 °C. Samples were taken at specific time intervals, filtered, and the remaining MV concentration was determined at 590 nm using a vis-spectrophotometer. Moreover, the point of zero charge ( $\text{pH}_{\text{pzc}}$ ) was determined using the Potentiometric Mass Titration (PMT) technique. The removal percentage of the dye and the adsorption capacity  $q_t$  were calculated using the following eqn (1) and (2):

$$R(\%) = \frac{(C_0 - C_t)}{C_0} \times 100, \quad (1)$$

$$q_t (\text{mg g}^{-1}) = \frac{(C_0 - C_t) \times V}{m}, \quad (2)$$

where  $C_0$  and  $C_t$  denote the concentrations of MV dye at  $t_0$  and at time  $t_t$ , respectively. The volume of the MV solution is indicated by  $V$  in L, and  $m$  represents the mass of  $\text{Ni}_{0.6}\text{Zn}_{0.2}\text{Sb}_{0.2}\text{FD}$  in g.

### 2.5. Recyclability test

The reusability of the  $\text{Ni}_{0.6}\text{Zn}_{0.2}\text{Sb}_{0.2}\text{FD}_{10}$  was determined during five consecutive MV removal processes. After each elimination process, the  $\text{Ni}_{0.6}\text{Zn}_{0.2}\text{Sb}_{0.2}\text{FD}_{10}$  adsorbent was

separated *via* its exhibited magnetic properties, rinsed with distilled water, and oven-dried at 60 °C for an overnight period. The resurrected adsorbent was subsequently used in subsequent removal operations.

## 3. Results and discussion

### 3.1. Characterization of the adsorbent

The samples were characterized, in a previously published work, using X-ray powder diffraction (XRD), transmission electron microscopy (TEM), energy dispersive X-ray analysis (EDX), and vibrating sample magnetometer (VSM). The results are summarized in Table 1.<sup>12</sup>

The lattice parameter ' $a$ ' is found to decrease with the increase in the dextrose monohydrate capping agent. This decrease in the lattice parameter with the presence of dextrose monohydrate is due to the improved crystallinity and reduction of nuclei of nanoferrites.<sup>12</sup> However, the crystallite size increases with the increase in dextrose monohydrate capping agent up to a maximum of 22.785 nm for sample  $\text{Ni}_{0.6}\text{Zn}_{0.2}\text{Sb}_{0.2}\text{FD}_{10}$ . Further increase in dextrose monohydrate concentration leads to a decrease in the crystallite size. This is explained on the basis that a concentration of 0.05 M and 0.1 M of dextrose monohydrate improves the crystallite growth in the synthesized samples, while the decrease obtained at higher dextrose monohydrate concentrations is a result of the excess amount of dextrose monohydrate absorbed on the surface of the nanoferrites.<sup>14,15</sup> Regarding the phase percentage, it is noted that the phase percentage of the nanoferrites increases while the phase percentage of hematite ( $\alpha\text{-Fe}_2\text{O}_3$ ) decreases with the increase in dextrose monohydrate concentration. This proves that the capping agent improves the formation of the  $\text{Ni}_{0.6}\text{Zn}_{0.2}\text{Sb}_{0.2}\text{FD}$  phase and retards the formation of the  $\alpha\text{-Fe}_2\text{O}_3$  phase.<sup>16,17</sup> The particle size obtained from TEM increases with the increase in the capping agent concentration up to a maximum of 16.773 nm for a dextrose monohydrate concentration of 0.1 M. Further increases in capping agent concentration cause a decrease in the particle size. The EDX patterns proved the presence of Ni, Zn, Sb, Fe, and O in all samples, in

Table 1 Summary of the results obtained from different characterization techniques<sup>12</sup>

Method of characterization	Parameter	$\text{Ni}_{0.6}\text{Zn}_{0.2}\text{Sb}_{0.2}\text{FD}_0$	$\text{Ni}_{0.6}\text{Zn}_{0.2}\text{Sb}_{0.2}\text{FD}_5$	$\text{Ni}_{0.6}\text{Zn}_{0.2}\text{Sb}_{0.2}\text{FD}_{10}$	$\text{Ni}_{0.6}\text{Zn}_{0.2}\text{Sb}_{0.2}\text{FD}_{20}$	$\text{Ni}_{0.6}\text{Zn}_{0.2}\text{Sb}_{0.2}\text{FD}_{35}$	
XRD	$a$ (Å)	8.361	8.360	8.360	8.357	8.356	
	Phase percentage of ferrite (%)	91.482	95.149	94.640	97.460	99.479	
	Phase percentage of hematite (%)	8.518	4.851	5.360	2.540	0.521	
	$D$ (nm)	18.334	20.543	22.785	17.692	16.367	
TEM	$D_{\text{TEM}}$ (nm)	15.402	16.516	16.773	15.320	15.258	
VSM	$M_s$ ( $\text{emu g}^{-1}$ )	35.836	39.757	39.416	40.813	39.503	
	$H_c$ (G)	25.981	36.845	39.501	35.644	29.814	
EDX	Average Theoretical			Average Theoretical			
	Ni:Fe	0.299	0.3	0.279	0.3	0.300	0.3
	Zn:Fe	0.084	0.1	0.087	0.1	0.092	0.1
	Sb:Fe	0.104	0.1	0.104	0.1	0.116	0.1
	O:Fe	2.292	2	2.089	2	2.811	2



addition to carbon (C) in dextrose monohydrate capped samples. Moreover, the atomic percentage of the different elements and their average ratios obtained from the different regions were similar and comparable to the theoretical ones. The obtained ratios are displayed in Table 1. The bulk dextrose monohydrate loading calculated from EDX is found to be in the range 5–8%, while the surface loading obtained from XPS is found to be in the range 15–17% according to the equations (a–c)<sup>18,19</sup> present below. The higher loading value obtained from XPS is explained on the basis that XPS is a surface-sensitive quantitative spectroscopic technique that measures the very topmost atoms. Since dextrose monohydrate is used as a capping agent, it forms a thin protective layer around the surface of the nanoferrites rather than being a bulk material. The saturation magnetization  $M_s$  values determined from VSM increase with the increase in dextrose monohydrate concentration to a maximum of 40.813 emu g<sup>-1</sup> for Ni<sub>0.6</sub>Zn<sub>0.2</sub>Sb<sub>0.2</sub>FD<sub>20</sub> sample. The decrease in hematite percentage and the variation in the crystallite size are the causes of the increase in  $M_s$  values. This proves the change in magnetic behaviour.<sup>20</sup> The increase in dextrose monohydrate concentration causes an increase in the coercivity  $H_c$  values to a maximum of 39.501 G for the Ni<sub>0.6</sub>-Zn<sub>0.2</sub>Sb<sub>0.2</sub>FD<sub>10</sub> sample. Further increase in capping agent concentration leads to a decrease in  $H_c$  values.

$$n_D = \frac{\text{atomic \% of C}}{\text{carbon atoms per formula unit}}, \quad (3)$$

$$n_{\text{ferrite}} = \frac{\sum \text{atomic \% of metals}}{\text{metal atoms per formula unit}}, \quad (4)$$

$$\begin{aligned} &\text{Dextrose monohydrate}(D)\text{loading ratio} \\ &= \frac{n_D \times M_D}{n_D \times M_D + n_{\text{ferrite}} \times M_{\text{ferrite}}} \times 100 \end{aligned} \quad (5)$$

### 3.2. UV-vis spectroscopy analysis

To measure the optical properties of the synthesized nanoparticles, UV-vis spectroscopy was used. The absorbance, transmittance, and reflectance spectra of uncapped and capped Ni<sub>0.6</sub>Zn<sub>0.2</sub>Sb<sub>0.2</sub>FD are represented in Fig. 1(a–c). A high absorption peak is observed in all samples in the range (330–334 nm).

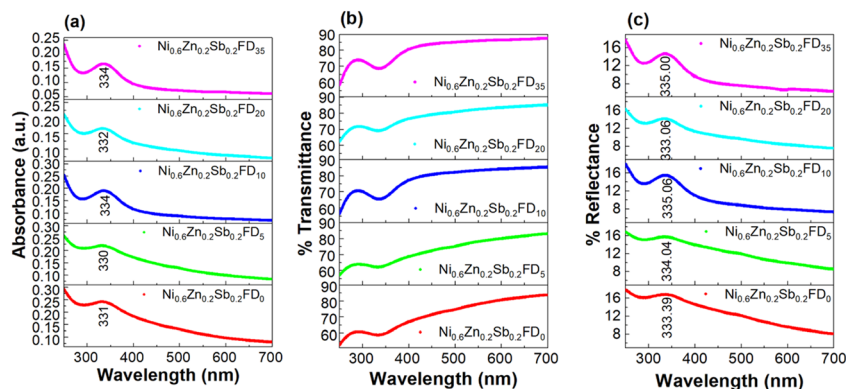


Fig. 1 The absorbance (a), transmittance (b), and reflectance (c) spectra of the uncapped and capped Ni<sub>0.6</sub>Zn<sub>0.2</sub>Sb<sub>0.2</sub>FD.

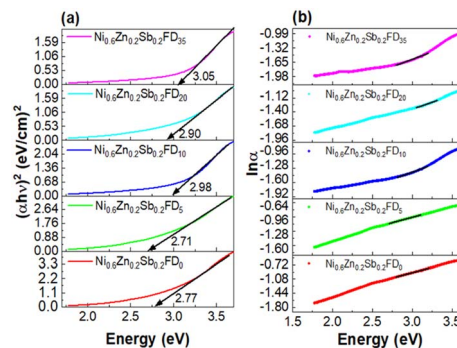


Fig. 2 Tauc plots (a) and Urbach energy (b) of the uncapped and capped Ni<sub>0.6</sub>Zn<sub>0.2</sub>Sb<sub>0.2</sub>FD.

The variation in this peak is related to the variation in energy bandgap ( $E_g$ ).<sup>21</sup> Previous studies investigated the UV-vis spectroscopy of NiFe<sub>2</sub>O<sub>4</sub> nanoparticles, where an absorption peak is observed at 338 nm by Kumari *et al.*<sup>22</sup> On the other hand, the absorption peak of ZnFe<sub>2</sub>O<sub>4</sub> is at 433 nm as investigated by Talebi *et al.*<sup>23</sup> The absorbance peak of Ni<sub>0.5</sub>Zn<sub>0.5</sub>Fe<sub>2</sub>O<sub>4</sub> is at 376 nm, as shown by Chehade *et al.*<sup>24</sup> However, the transmittance follows an opposite trend to that of absorbance, where the transmittance is minimum in the UV region and increases with the increase in wavelength, so that the maximum is obtained in the visible region. The reflectance, represented in Fig. 1(c), follows the same trend as that of absorbance. The maximum reflectance appears in the UV region, while the minimum occurs in the visible region. Upon the increase in dextrose monohydrate capping agent concentration, the reflectance decreases. Therefore, the synthesized nanoparticles can be utilized in transparent electrodes and optoelectronic devices.<sup>21</sup>

The direct energy gap of the synthesized uncapped and capped nanoferrites is extracted from Tauc plots, provided in Fig. 2(a), and calculated according to the following eqn (6):<sup>21</sup>

$$(\alpha hv)^n = B(hv - E_g), \quad (6)$$

where  $\alpha$  is the absorption coefficient  $\alpha = 2.303 \frac{A}{t}$   $A$  is the absorbance, and  $t$  is the sample thickness.<sup>25</sup>  $h\nu$  is the excitation energy,  $B$  is a constant,  $E_g$  is the energy gap, and  $n$  is a constant



that depends on the type of transition. Here,  $n$  is taken to be equal to 2 for the allowed direct transition. The crystallite size, the lattice parameters, the degree of stoichiometry, the substituted elements, the cation distribution, and the presence of impurities are factors that affect the value of  $E_g$ .<sup>21</sup> The  $E_g$  values decreased with the addition of dextrose monohydrate in sample  $\text{Ni}_{0.6}\text{Zn}_{0.2}\text{Sb}_{0.2}\text{FD}_5$  till 2.71 eV and then increased with the increase in dextrose monohydrate concentration till reaching a value of 3.05 eV for  $\text{Ni}_{0.6}\text{Zn}_{0.2}\text{Sb}_{0.2}\text{FD}_{35}$  sample. Thus,  $E_g$  values are not greatly affected by the concentration of the capping agent. The variation in the  $E_g$  values is due to the perturbations occurring in the electronic structure upon introducing the dextrose monohydrate as a capping agent.

To determine the band tail width of the localized states, the Urbach energy was calculated using eqn (7):

$$\alpha = \beta \exp\left(\frac{h\nu}{E_u}\right), \quad (7)$$

where  $\beta$  is a constant and  $E_u$  is the Urbach energy, which measures the disorder in the structure of the synthesized nanoferrites. The  $E_u$  values are obtained by plotting  $\ln(\alpha)$  versus  $h\nu$  as shown in Fig. 2(b), where  $E_u$  is equal to the reciprocal of the slope. As shown in Fig. 3, the  $E_u$  values vary between 1.46 and 2.08 eV in the presence of dextrose monohydrate capping agent. The addition of dextrose monohydrate capping agent causes a decrease in  $E_u$  values except for  $\text{Ni}_{0.6}\text{Zn}_{0.2}\text{Sb}_{0.2}\text{FD}_5$ . Therefore, the addition of the capping agent leads to a decrease in defects and disorder represented by the decrease in  $E_u$  values

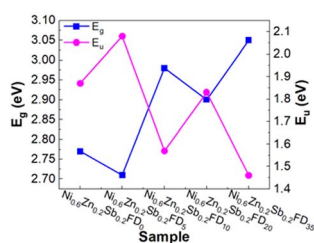


Fig. 3 The variation of  $E_g$  and  $E_u$  of  $\text{Ni}_{0.6}\text{Zn}_{0.2}\text{Sb}_{0.2}\text{FD}$  capped with different concentrations of dextrose monohydrate.

and, consequently, an increase in  $E_g$  values, except in the  $\text{Ni}_{0.6}\text{Zn}_{0.2}\text{Sb}_{0.2}\text{FD}_5$  sample, as displayed in Fig. 3. Thus,  $E_u$  and  $E_g$  have an inverse behaviour, following the general trend. Hence, the synthesized samples, especially  $\text{Ni}_{0.6}\text{Zn}_{0.2}\text{Sb}_{0.2}\text{FD}_5$ , with the lowest  $E_g$ , are suitable for photocatalytic activity and optoelectronic devices.<sup>26–28</sup>

The skin depth  $\delta$ , the optical density  $D_{\text{opt}}$ , and the extinction coefficient  $k$  of the synthesized nanoferrites are calculated according to the following eqn (8)–(10).<sup>25,29,30</sup>

$$\delta = \frac{1}{\alpha}, \quad (8)$$

$$D_{\text{opt}} = \alpha \times t, \text{ and} \quad (9)$$

$$k = \frac{\alpha\lambda}{4\pi c}, \quad (10)$$

where  $\lambda$  is the wavelength. As depicted in Fig. 4(a and b), the skin depth of the synthesized nanoferrites increases, while the optical density decreases upon the increased addition of dextrose monohydrate capping agent. This variation in optical density is due to a decrease in absorption.<sup>30</sup> The extinction coefficient is an indication of the amount of energy dissipated by the synthesized nanoferrites due to the absorption and scattering phenomena.<sup>31</sup> As shown in Fig. 4(c), the extinction coefficient decreases with the increase in the wavelength, and the highest value of the extinction coefficient is obtained in the wavelength range 340–345 nm. This decrease in  $k$  upon the increase in wavelength indicates the decrease in the fraction of light lost as a result of absorbance and scattering in this region.<sup>32</sup> Also, the reduction of  $k$  in the visible region proves the elevation of transmittance in this region.<sup>24</sup> It is also observed that upon the addition of a dextrose monohydrate capping agent and the increase in its concentration, the extinction coefficient decreases. These results show that the samples are suitable for application in optoelectronic devices.<sup>33</sup>

The refractive index  $n$  is one of the most fundamental parameters for materials applicable in optical domains such as optical sensors, switches, modulators, and optical filters. To calculate the refractive index, eqn (11) is used:<sup>33</sup>

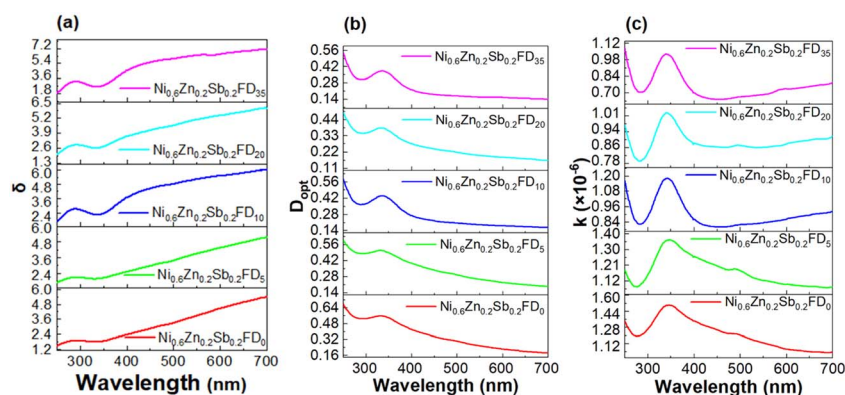


Fig. 4 The variation of (a)  $\delta$ , (b)  $D_{\text{opt}}$ , and (c) the extinction coefficient as a function of the wavelength of the uncapped and capped  $\text{Ni}_{0.6}\text{Zn}_{0.2}\text{Sb}_{0.2}\text{FD}$ .



$$n = \left[ \frac{1+R}{1-R} \right] + \left[ \frac{4 \times R}{(1-R)^2} - k^2 \right]^{1/2} \quad (11)$$

where  $R$  is the reflectance and  $k$  is the extinction coefficient. The refractive index values obtained are presented in Fig. 5. The refractive index calculated using the mentioned method varies between 2.21 and 2.39. The refractive index value decreases upon the addition of different concentrations of the capping agent and is comparable to those obtained in the literature.<sup>33,34</sup> This indicates that the synthesized  $\text{Ni}_{0.6}\text{Zn}_{0.2}\text{Sb}_{0.2}\text{FeD}$  nanoferrites can be used in optoelectronic, solar, and technological applications.<sup>33,34</sup>

The real dielectric constant  $\epsilon_r$ , the imaginary dielectric constant  $\epsilon_i$ , and the dielectric loss factor  $\tan \delta$ , which indicates the depletion of the electrical energy, can be determined from the refractive index and the extinction coefficient according to the following eqn (12)–(14):<sup>30,33</sup>

$$\epsilon_r = n^2 - k^2, \quad (12)$$

$$\epsilon_i = 2nk, \quad (13)$$

$$\tan \delta = \frac{\epsilon_i}{\epsilon_r}, \quad (14)$$

$\epsilon_r$  shows the extent to which the material will reduce the speed of light, while  $\epsilon_i$  indicates how the dielectric material absorbs energy from an electric field as a result of the dipole

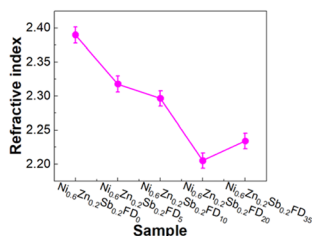


Fig. 5 The refractive index for the uncapped and capped  $\text{Ni}_{0.6}\text{Zn}_{0.2}\text{Sb}_{0.2}\text{FD}$ .

motion.<sup>33</sup> The variation of  $\epsilon_r$ ,  $\epsilon_i$ , and  $\tan \delta$  as a function of wavelength is displayed in Fig. 6(a–c), respectively. As observed,  $\epsilon_r$ ,  $\epsilon_i$ , and  $\tan \delta$  values are almost decreasing with the increase in the wavelength. At low wavelength, a maximum is observed in the range 334–336 nm for  $\epsilon_r$ , while the maximum of  $\epsilon_i$  is found to be in the range 337–342 nm, and that of  $\tan \delta$  is in the range 343–348 nm. The high value of  $\epsilon_r$  and  $\epsilon_i$  at low wavelengths signifies an insulating behaviour.<sup>33</sup> The addition of dextrose monohydrate capping agent and the increase in its concentration cause a decrease in  $\epsilon_r$ ,  $\epsilon_i$ , and  $\tan \delta$ .

The optical conductivity  $\sigma_{\text{opt}}$  and electric conductivity  $\sigma_e$  are calculated using the following eqn (15) and (16):<sup>25</sup>

$$\sigma_{\text{opt}} = \frac{\alpha nc}{4\pi}, \quad (15)$$

$$\sigma_e = \frac{2\lambda\sigma_{\text{opt}}}{\alpha}, \quad (16)$$

where  $c$  is the speed of light in a vacuum.

The variation of  $\sigma_{\text{opt}}$  and  $\sigma_e$  as a function of the wavelength is present in Fig. 7(a and b). It is clear that  $\sigma_{\text{opt}}$  attained a maximum in the wavelength range 331–335 nm, then decreased with the increase in wavelength to attain a minimum in the visible region. However,  $\sigma_e$  increases with the increase in wavelength.  $\sigma_{\text{opt}}$  is directly proportional to the refractive index

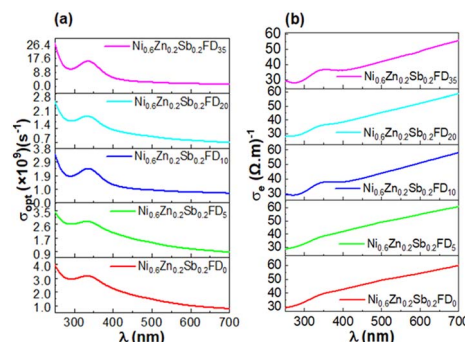


Fig. 7 The variation of  $\sigma_{\text{opt}}$  (a) and  $\sigma_e$  (b) as a function of the wavelength of the uncapped and capped  $\text{Ni}_{0.6}\text{Zn}_{0.2}\text{Sb}_{0.2}\text{FD}$ .

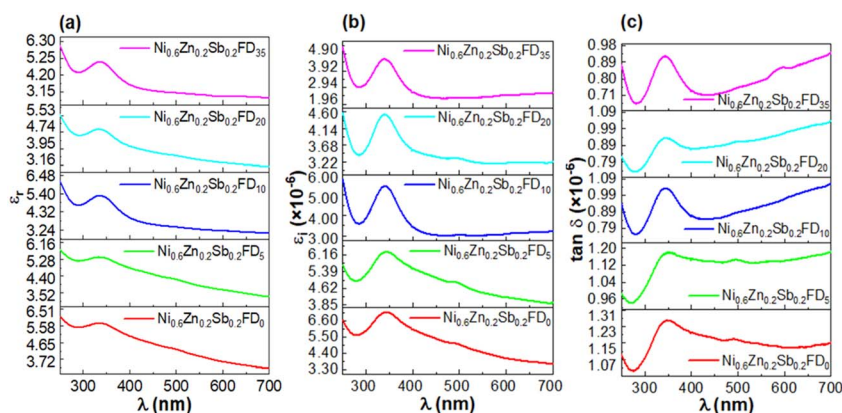


Fig. 6 The variation of the real dielectric constant (a), the imaginary dielectric constant (b), and the dielectric loss factor (c) versus wavelength of the uncapped and capped  $\text{Ni}_{0.6}\text{Zn}_{0.2}\text{Sb}_{0.2}\text{FD}$ .



and the absorption coefficient. The increase in  $\sigma_{\text{opt}}$  in the wavelength range 331–335 nm is due to the increase in the absorption coefficient in this range and the increase in the excitation of electrons.<sup>29</sup> Also,  $\sigma_e$  values are much lower than  $\sigma_{\text{opt}}$  as a result of a deficiency in the energy needed for the free carriers to jump the potential barrier level.<sup>33</sup> This renders the synthesized nanoferrites as potential candidates in optoelectronic devices.<sup>33</sup>

### 3.3. Determination of $E_0$ , $E_d$ , $S_0$ , $\lambda_0$ , $\epsilon_1$ and $\gamma$

Wemple and Di Domenico's relationship eqn (17) expresses the dispersion of the refractive index in the synthesized nanoferrites using the concept of the single oscillator:<sup>33</sup>

$$(n^2 - 1)^{-1} = \frac{E_0}{E_d} - \frac{1}{E_0 E_d} (h\nu)^2, \quad (17)$$

where  $E_0$  is the oscillator energy and  $E_d$  is the dispersion energy, which measures the average strength of interband optical energy.

Fig. 8(a) displays the linear fit of  $(n^2 - 1)^{-1}$  versus  $(h\nu)^2$ . The obtained values are listed in Table 2, where  $E_0$  and  $E_d$  can be determined using the slope  $\left(\frac{1}{E_0 E_d}\right)$  and the intercept  $\frac{E_0}{E_d}$ .  $E_0$  is related to the optical band gap energy by the following equation:  $E_0 \approx \gamma E_g$ . Where  $\gamma$  is a coefficient of proportionality and is approximately equal to 2. The slight variation between  $E_g$  obtained from Tauc plot and  $E_g$  calculated from Wemple and Di Domenico's relation is due to the difference in the region used for performing the calculation.<sup>35</sup> The transparent region of the spectrum is used for calculation in Wemple and Di Domenico's relation, while in Tauc plot, the absorption region is used.

The single term Sellmeier oscillation expresses the variation of the refractive index as a function of wavelength according to the following eqn (18):<sup>35</sup>

$$n^2 - 1 = \frac{S_0 \lambda_0^2}{1 - \left(\frac{\lambda_0}{\lambda}\right)^2}, \quad (18)$$

where  $S_0$  is the average oscillator strength,  $\lambda_0$  is the average oscillator wavelength, and  $\lambda$  is the wavelength of the incident light. The plot of  $(n^2 - 1)^{-1}$  versus  $\lambda^{-2}$  is present in Fig. 8(b). The values of  $S_0$  and  $\lambda_0$  are obtained from the slope and intercept of the curve present in Fig. 8(b) and are listed in Table 2. As shown,  $S_0$  and  $\lambda_0$  values are found to vary with the addition of a dextrose monohydrate capping agent and the increase in its concentration. The highest value of  $\lambda_0$  in the presence of the capping agent is found to be 284 nm for  $\text{Ni}_{0.6}\text{Zn}_{0.2}\text{Sb}_{0.2}\text{FD}_{3.5}$ .

The lattice dielectric constant  $\epsilon_1$  is determined to obtain more information on the optical properties of the synthesized nanoparticle using the following eqn (19):<sup>33</sup>

$$n^2 = \epsilon_1 - \gamma \lambda^2 \quad (19)$$

where  $\gamma$  is a constant.  $\epsilon_1$  value is the intercept with the vertical axis obtained by extrapolating the linear part toward a shorter wavelength, as present in Fig. 8(c). The values are tabulated in Table 2. As shown in Table 2,  $\epsilon_1$  values decrease with the addition of a dextrose monohydrate capping agent and with the increase in its concentration.

The calculated parameters present in Table 2 are found to be influenced by the concentration of the capping agent, indicating that the capping agent helps improve the optical

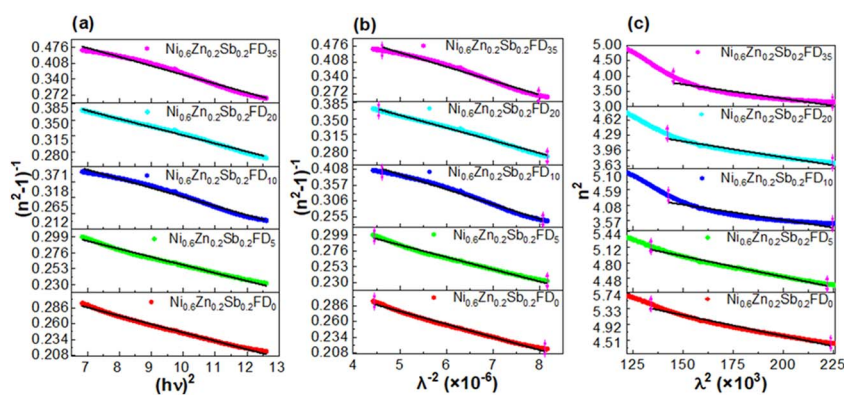


Fig. 8 The linear fit of (a)  $(n^2 - 1)^{-1}$  versus  $(h\nu)^2$ , (b)  $(n^2 - 1)^{-1}$  versus  $\lambda^{-2}$ , and (c)  $n^2$  versus  $\lambda^2$  of the uncapped and capped  $\text{Ni}_{0.6}\text{Zn}_{0.2}\text{Sb}_{0.2}\text{FD}$ .

Table 2 The values of the optical parameters of the uncapped and capped  $\text{Ni}_{0.6}\text{Zn}_{0.2}\text{Sb}_{0.2}\text{FD}$

Sample	$E_0$ (eV)	$E_d$ (eV)	$S_0$ ( $\text{m}^{-2}$ )	$\lambda_0$ (nm)	$\epsilon_1$	$\gamma$
$\text{Ni}_{0.6}\text{Zn}_{0.2}\text{Sb}_{0.2}\text{FD}_0$	5.28	13.80	$4.71 \times 10^{-5}$	236	6.80	$1.09 \times 10^{-5}$
$\text{Ni}_{0.6}\text{Zn}_{0.2}\text{Sb}_{0.2}\text{FD}_5$	5.69	15.22	$5.63 \times 10^{-5}$	218	6.20	$8.44 \times 10^{-6}$
$\text{Ni}_{0.6}\text{Zn}_{0.2}\text{Sb}_{0.2}\text{FD}_{10}$	4.53	7.28	$2.09 \times 10^{-5}$	275	5.62	$1.01 \times 10^{-5}$
$\text{Ni}_{0.6}\text{Zn}_{0.2}\text{Sb}_{0.2}\text{FD}_{20}$	5.25	10.57	$3.57 \times 10^{-5}$	237	5.18	$6.85 \times 10^{-6}$
$\text{Ni}_{0.6}\text{Zn}_{0.2}\text{Sb}_{0.2}\text{FD}_{35}$	4.41	5.95	$1.65 \times 10^{-5}$	284	5.12	$9.30 \times 10^{-6}$



properties of the synthesized samples and consequently boosts their integration in optoelectronic applications.<sup>33</sup>

### 3.4. Photoluminescence spectroscopy (PL)

Photoluminescence spectroscopy is a technique used to study the optical properties of nanoparticles and investigate the interstitial defects and the recombination process of electrons.<sup>36</sup> PL studies on the synthesized nanoferrites were done at room temperature using 5 different excitation wavelengths (315, 330, 345, 360, and 370 nm) and are displayed in Fig. 9. As shown in Fig. 9, the spectra are divided into two regions: UV emission and visible emission. The intensity of the UV emission is higher compared to that of the visible emissions. This proves the excellent crystal quality of the synthesized nanoferrites and proposes their use in nano-optoelectronic devices.<sup>37</sup> The peaks appearing in the UV region at all excitation wavelengths correspond to the near band edge emission, corresponding to the direct recombination of electrons trapped in oxygen vacancies with photogenerated holes.<sup>38</sup> As shown in the inset of Fig. 9, the intensity of the peaks decreases with the increase in the excitation wavelength. This behavior is due to the enhancement of photogenerated electron-hole pairs at shorter wavelengths.<sup>37</sup> Therefore, the synthesized samples can be utilized in light-emitting devices.<sup>37</sup> Also, there is a red shift in the position of the peaks as a result of the selective particle size distribution in the synthesized nanoferrites due to polydispersion.<sup>39</sup>

The CIE 1931 chromaticity diagrams of the uncapped and capped  $\text{Ni}_{0.6}\text{Zn}_{0.2}\text{Sb}_{0.2}\text{FD}$  at different excitation wavelengths are

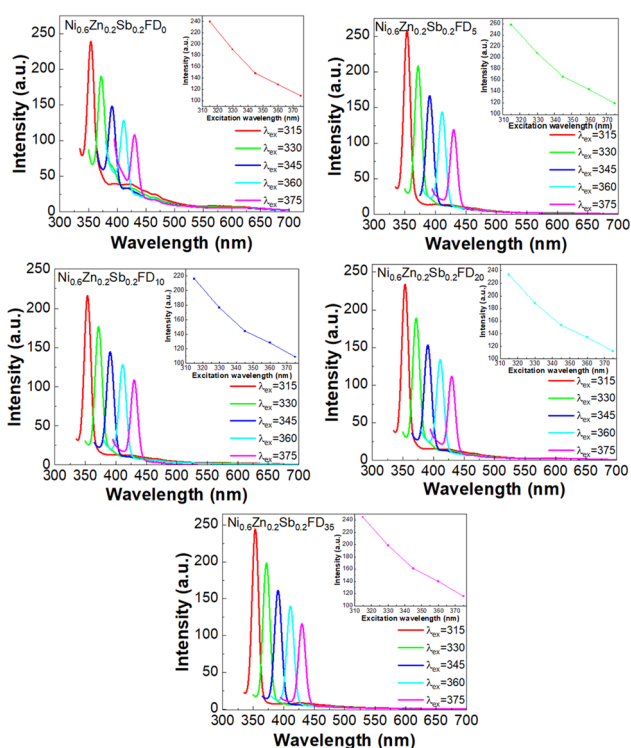


Fig. 9 PL curves of the uncapped and capped  $\text{Ni}_{0.6}\text{Zn}_{0.2}\text{Sb}_{0.2}\text{FD}$  at different excitation wavelengths.

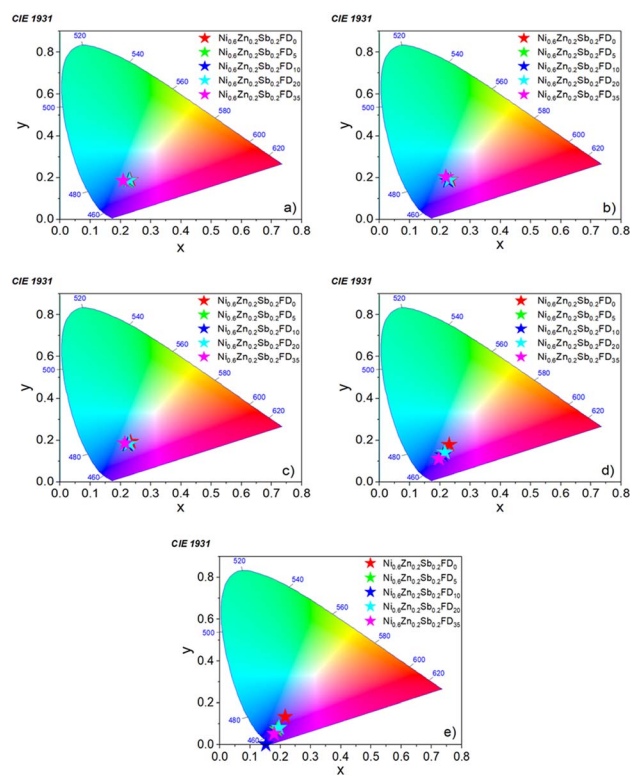


Fig. 10 The CIE 1931 chromaticity diagrams of the uncapped and capped  $\text{Ni}_{0.6}\text{Zn}_{0.2}\text{Sb}_{0.2}\text{FD}$  at different excitation wavelengths: (a) 315, (b) 330, (c) 345, (d) 360, and (e) 375 nm.

depicted in Fig. 10. These diagrams are used to determine the color tenability and the luminescent behavior of the synthesized nanoferrites.<sup>37</sup> This is done by calculating the color coordinates ( $x, y$ ) of the emission spectra of the prepared samples. As displayed in the CIE diagrams, the coordinates of all samples are found in the blue region, signifying that the prepared nanoferrites can be utilized as a source of blue-chip light and near-UV white light-emitting diode devices.

### 3.5. $\text{Ni}_{0.6}\text{Zn}_{0.2}\text{Sb}_{0.2}\text{FD}_{10}$ adsorbent performance

**3.5.1 Optimization of adsorbent components.** To assess the adsorptive capability of dextrose monohydrate ( $D$ ) in  $\text{Ni}_{0.6}\text{Zn}_{0.2}\text{Sb}_{0.2}\text{FD}$ , a comparative test was conducted between the removal efficacy of MV by different incorporated concentrations of  $D$  at 0, 0.05, 0.1, 0.2, and 0.35 M, corresponding to  $D_0, D_5, D_{10}, D_{20}$ , and  $D_{35}$ , as depicted in Fig. 11(a). On increasing  $D$  molar concentration in the adsorbent from 0 to 0.1 M, the MV removal efficacy and adsorption capacity boosted after 60 min from 32.9% and 31.6  $\text{mg g}^{-1}$  to 78.5% and 75.5  $\text{mg g}^{-1}$ , respectively. This was attributed to the enhancement of adsorptive active sites. Whereas, the removal percentage and adsorption capacity declined to 64.3% and 61.9  $\text{mg g}^{-1}$  in 0.35 M  $D$  after 60 min due to the blockage occurring at active sites in the adsorbent. Hence, the primary concentration of  $D$  was 0.1 M and exhibited higher values of  $q_{\text{max}}$  capacity and % $R$  compared to the other samples, which were used for all studies. This is because  $\text{Ni}_{0.6}\text{Zn}_{0.2}\text{Sb}_{0.2}\text{FD}_{10}$  sample has the largest size compared to the



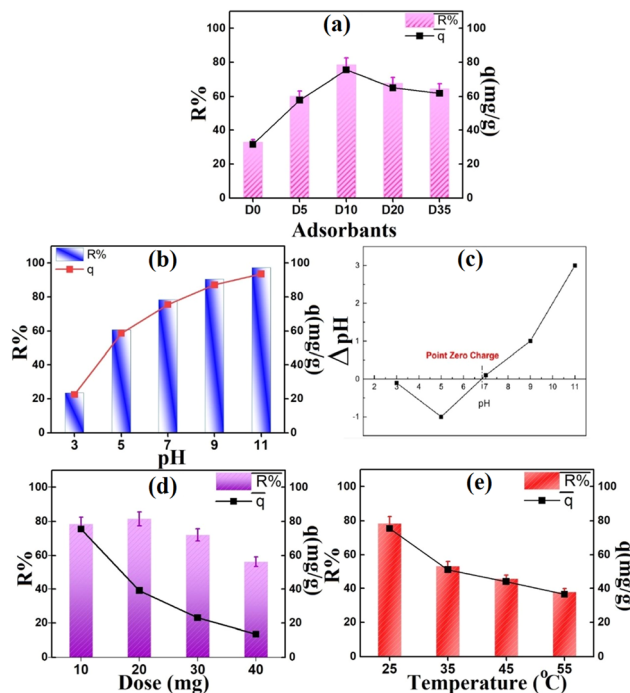


Fig. 11 (a) Comparative study between the adsorption performance of the uncapped and capped  $\text{Ni}_{0.6}\text{Zn}_{0.2}\text{Sb}_{0.2}\text{FD}_{10}$ , (b) impact of pH, (c) the zero-point charge diagram, (d) impact of  $\text{Ni}_{0.6}\text{Zn}_{0.2}\text{Sb}_{0.2}\text{FD}_{10}$  dosage, and (e) impact of temperature on MV removal (Exp. conditions; MV =  $10 \text{ mg L}^{-1}$ , adsorbent dose =  $0.01 \text{ g}$ , pH = 7, and an equilibrium time = 60 min).

other samples, an  $E_g$  value = 2.98 eV, and an Urbach energy = 1.57 eV. The band gap energy and Urbach energy values indicate effective defect passivation and structural ordering, thus having a better removal efficiency and higher adsorption capacity compared to other samples.<sup>27</sup> Moreover, a moderate dextrose monohydrate concentration decreases agglomeration and ensures an ordered surface structure having hydroxyl groups that form electrostatic interactions with the cationic MV dye.<sup>40</sup>

**3.5.2 The impact of different experimental factors on MV removal.** To determine the best conditions for the removal of MV dye, several experimental factors were tested. These factors include the effect of pH, the effect of  $\text{Ni}_{0.6}\text{Zn}_{0.2}\text{Sb}_{0.2}\text{FD}_{10}$  dosage, the effect of temperature, the effect of time, and the effect of MV initial concentration. Moreover, the recyclability test was carried out to study the ability to reuse and regenerate the adsorbent.

**3.5.3 Assessing the influence of the pH factor.** The pH of the medium plays a crucial role in controlling the MV removal. It significantly affects the protonation or deprotonation of functional groups on adsorbent and adsorbate surfaces in solution. The adsorbability of  $\text{Ni}_{0.6}\text{Zn}_{0.2}\text{Sb}_{0.2}\text{FD}_{10}$  sample to MV was studied at pH ranges 3–11, as shown in Fig. 11(b). The MV removal percentage and adsorption capacity elevated from 23.4% and  $22.5 \text{ mg g}^{-1}$  to 98.7% and  $95.9 \text{ mg g}^{-1}$ , corresponding to pH 3 to 11, respectively. This was confirmed by studying  $\text{Ni}_{0.6}\text{Zn}_{0.2}\text{Sb}_{0.2}\text{FD}_{10}$  adsorbent surface charge as shown in Fig. 11(c). The decreased removal percent of MV cationic dye

at low pHs may be due to electrostatic repulsion between the positively charged cationic MV dye and the positively charged  $\text{Ni}_{0.6}\text{Zn}_{0.2}\text{Sb}_{0.2}\text{FD}_{10}$  surface (since at  $\text{pH} < 6.8$ , the surface is protonated).<sup>41</sup> Besides, the high concentration of  $\text{H}^+$  ions in the medium competes with MV molecules for the occupation of  $\text{Ni}_{0.6}\text{Zn}_{0.2}\text{Sb}_{0.2}\text{FD}_{10}$  active sites. At neutral pH ( $\text{pH} = \text{pH}_{\text{pzc}} = 6.8$ ), the reduction in  $\text{H}^+$  ions in the medium diminishes the electrostatic repulsion and competition between protons and MV molecules on  $\text{Ni}_{0.6}\text{Zn}_{0.2}\text{Sb}_{0.2}\text{FD}_{10}$  adsorbent, leading to an enhanced MV removal value at  $\text{pH} = 7$ .<sup>42</sup> Whereas, at high pHs ( $\text{pH} > \text{pH}_{\text{pzc}}$ ), the significant shift in MV removal%, reaching 98.7% at pH 11.0, was attributed to the deprotonation that occurred to  $\text{Ni}_{0.6}\text{Zn}_{0.2}\text{Sb}_{0.2}\text{FD}_{10}$ , leaving a negative charge on  $\text{Ni}_{0.6}\text{Zn}_{0.2}\text{Sb}_{0.2}\text{FD}_{10}$  surface that enhances the electrostatic attraction between the adsorbent and the cationic MV molecules. Moreover, Duynstee and Grunwald<sup>43</sup> found that MV dye and  $\text{OH}^-$  ions interacted in the pH range of 9.0 to 13.0. Where these hydroxyl ions strike the MV molecule's core carbon atom, resulting in a base carbinol with a unique chemical structure that enhances the removal. Thus, we chose the optimal pH at 7 in our conducted experiments to ensure the role of  $\text{Ni}_{0.6}\text{Zn}_{0.2}\text{Sb}_{0.2}\text{FD}_{10}$  surface on adsorption rather than  $\text{OH}^-$  ions.

### 3.5.4 Assessing the influence of $\text{Ni}_{0.6}\text{Zn}_{0.2}\text{Sb}_{0.2}\text{FD}_{10}$ dose.

The impact of varying the  $\text{Ni}_{0.6}\text{Zn}_{0.2}\text{Sb}_{0.2}\text{FD}_{10}$  dosage on the MV adsorption was investigated. Fig. 11(d) shows the MV removal% at the dosage ranging from 10 to 40 mg  $\text{Ni}_{0.6}\text{Zn}_{0.2}\text{Sb}_{0.2}\text{FD}_{10}$ . The removal efficiency rose from 78.5% to 81.5% as the adsorbent dose increased from 10 to 20 mg. This rise can be explained by enhancing the  $\text{Ni}_{0.6}\text{Zn}_{0.2}\text{Sb}_{0.2}\text{FD}_{10}$  surface area and the availability of adsorption sites. On the contrary, the decline in adsorption capacity from 72.1% to 56.3%, which corresponds to a 30 to 40 mg  $\text{Ni}_{0.6}\text{Zn}_{0.2}\text{Sb}_{0.2}\text{FD}_{10}$  dose, might result from minimizing the surface area and hence the active adsorption sites due to particle aggregation.<sup>44</sup> It was also shown that increasing  $\text{Ni}_{0.6}\text{Zn}_{0.2}\text{Sb}_{0.2}\text{FD}_{10}$  dose reduced the quantity of adsorbed MV per unit mass of adsorbent from 75.5 to  $13.5 \text{ mg g}^{-1}$ . With increasing adsorbent mass,  $q_e$  ( $\text{mg g}^{-1}$ ) falls due to a split in the concentration gradient between MV concentration in the solution and on the  $\text{Ni}_{0.6}\text{Zn}_{0.2}\text{Sb}_{0.2}\text{FD}_{10}$  surface.<sup>5</sup>

**3.5.5 Assessing the influence of temperature.** To investigate how temperature affects MV adsorption efficiency, tests were conducted at optimal circumstances and temperatures ranging from 25–55 °C, Fig. 11(e). The MV adsorption % reduced from 78.5% to 38.0% with rising temperatures of 25–55 °C. The adsorption efficiency reduced with higher temperatures due to various factors, including the MV molecules detaching from the  $\text{Ni}_{0.6}\text{Zn}_{0.2}\text{Sb}_{0.2}\text{FD}_{10}$  surface and releasing into the solution. The changes and suppression in active sites, as well as the greater movement of MV molecules, occurred. These results and their interpretations are in agreement with findings reported in previous studies by Ahmadi A. *et al.*,<sup>45</sup> Changzhen Li *et al.*,<sup>46</sup> and Foroutan R. *et al.*<sup>42</sup> Thus, the optimal temperature for MV elimination is 25 °C, which also yields the highest efficiency at 78.5%.

**3.5.6 Influence of contact time.** Fig. 12(a) illustrates the impact of contact time on the amount of adsorbed MV on the  $\text{Ni}_{0.6}\text{Zn}_{0.2}\text{Sb}_{0.2}\text{FD}_{10}$  surface. It was observed that the initial



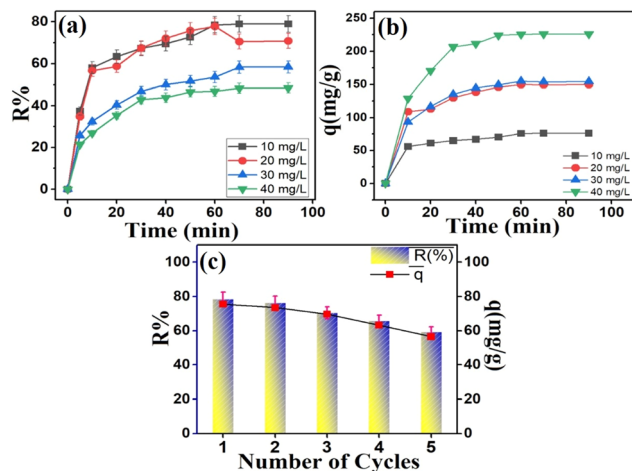


Fig. 12 (a) Effect of contact time, (b) the effect of the initial concentration of MV, and (c) the recyclability test of  $\text{Ni}_{0.6}\text{Zn}_{0.2}\text{Sb}_{0.2}\text{FD}_{10}$ .

stages of the adsorption process resulted in a swift rise in elimination, reaching  $55.8 \text{ mg g}^{-1}$ , corresponding to a maximum removal% at 58.2% in 10 min. Then, after the adsorption of MV on  $\text{Ni}_{0.6}\text{Zn}_{0.2}\text{Sb}_{0.2}\text{FD}_{10}$  was slowly increased until it attained the equilibrium time of 60 min, reaching a removal% and adsorption capacity of 78.5% and  $75.5 \text{ mg g}^{-1}$ , respectively. The initial high MV removal% may be due to the abundance of unoccupied sites on the  $\text{Ni}_{0.6}\text{Zn}_{0.2}\text{Sb}_{0.2}\text{FD}_{10}$  adsorbent. However, beyond the equilibrium time of 60 min, there is no noticeable removal effect since the number of available active sites was reduced due to saturation with MV dye molecules, as well as the electrostatic repulsive force between MV molecules was attained.<sup>47</sup>

**3.5.7 Influence of MV initial concentration.** Fig. 12(b) portrays the MV dose-altering effect on the adsorption capability of  $\text{Ni}_{0.6}\text{Zn}_{0.2}\text{Sb}_{0.2}\text{FD}_{10}$ . After 60 min, MV removal efficiency declined from 78.5% with MV concentration of  $10 \text{ mg L}^{-1}$  to 46.8% with increasing MV concentration to  $40 \text{ mg L}^{-1}$ . This was attributed to the higher MV concentrations causing more adsorption and adhesion of MV molecules on  $\text{Ni}_{0.6}\text{Zn}_{0.2}\text{Sb}_{0.2}\text{FD}_{10}$  surface, leading to its active sites' obstruction.<sup>48</sup> Besides, the experimental  $\text{Ni}_{0.6}\text{Zn}_{0.2}\text{Sb}_{0.2}\text{FD}_{10}$  dosage condition was the same, even in higher MV concentrations.<sup>44</sup> There was a reverse trend regarding the relationship between dye concentration and the adsorption capacity. Hence, the rise in dye concentration enhances the adsorption capacity as it increases the interaction between the adsorbate and the adsorbent. It was noticed in Fig. 12(b) that the spike in adsorption capacity from  $75.5$  to  $225.3 \text{ mg g}^{-1}$  when the MV concentration rose from 10 to  $40 \text{ mg L}^{-1}$  after 60 min. Increasing MV concentration can amplify its driving power, making the mass transfer easier, and allowing MV molecules to migrate from the bulk to the  $\text{Ni}_{0.6}\text{Zn}_{0.2}\text{Sb}_{0.2}\text{FD}_{10}$  surface.<sup>5</sup>

### 3.6. Recyclability test

The ability to reuse and regenerate the adsorbent is an essential factor since it allows the conservation and sustainability of

materials, provokes more applications, protects the environment, and is cost-effective.<sup>49,50</sup> So, it is important to assess the recyclability test for  $\text{Ni}_{0.6}\text{Zn}_{0.2}\text{Sb}_{0.2}\text{FD}_{10}$  sample. Therefore, the recyclability of  $\text{Ni}_{0.6}\text{Zn}_{0.2}\text{Sb}_{0.2}\text{FD}_{10}$  sample was tested over 5 cycles. The adsorption capacity was measured after each cycle to assess any decline in performance. The recyclability test, depicted in Fig. 12(c), highlighted a decrease in MV adsorption from 78.5% and  $75.6 \text{ mg g}^{-1}$  to 69.3% and  $66.7 \text{ mg g}^{-1}$ , respectively, after the 5th cycle. This outcome signified the stability of  $\text{Ni}_{0.6}\text{Zn}_{0.2}\text{Sb}_{0.2}\text{FD}_{10}$  and demonstrated strong regenerative properties. Moreover, the slight decrease in MV adsorption and removal percentage after repeated usage and regeneration was due to the partial blockage and some collapse of  $\text{Ni}_{0.6}\text{Zn}_{0.2}\text{Sb}_{0.2}\text{FD}_{10}$  active sites by MV molecules.<sup>51</sup>

### 3.7. Kinetic study

To explore the controlling mechanism of MV adsorption onto  $\text{Ni}_{0.6}\text{Zn}_{0.2}\text{Sb}_{0.2}\text{FD}_{10}$ , the experimental data were analyzed using pseudo-first-order (PFO), pseudo-second-order (PSO), Elovich models, and the intra-particle diffusion (IPD) model represented by eqn (20)–(23):<sup>52,53</sup>

$$\ln(q_e - q_t) = \ln q_e - k_1(t) \text{ (PFO)}, \quad (20)$$

$$\frac{t}{q_t} = \frac{1}{k_2 q_e^2} + \frac{t}{q_e} \text{ (PSO)}, \quad (21)$$

$$q_t = \frac{1}{\beta} \ln(\alpha\beta) + \frac{1}{\beta} \ln(t) \text{ (Elovich)}, \text{ and} \quad (22)$$

$$q_t = k_i t^{1/2} + C \text{ (IPD)}. \quad (23)$$

where  $q_e$  represents the amount of MV that adsorbs onto  $\text{Ni}_{0.6}\text{Zn}_{0.2}\text{Sb}_{0.2}\text{FD}_{10}$  at equilibrium, while  $q_t$  expresses the amount of MV adsorption at time  $t$ .  $k_1$  is the rate constant of the pseudo-first-order, and  $k_2$  is the rate constant pseudo-second-order.  $\alpha$  and  $\beta$  are Elovich coefficients that represent the initial adsorption rate and the desorption coefficient, respectively, and also relate to the extent of surface coverage and activation energy for chemisorption.  $K_i$  is the IPD constant ( $\text{mg g}^{-1} \text{ min}^{0.5}$ ), and  $C$  is the intercept ( $\text{mg g}^{-1}$ ).

The linear relationships derived from the previously mentioned models are presented in Fig. 13(a–d) and Table 3. The removal of MV by uncapped  $\text{Ni}_{0.6}\text{Zn}_{0.2}\text{Sb}_{0.2}\text{FD}_0$  is best fitted by PFO ( $R^2 = 0.95$ ). Whereas, the adsorption of MV onto capped  $\text{Ni}_{0.6}\text{Zn}_{0.2}\text{Sb}_{0.2}\text{FD}$  by different dextrose concentrations ( $D_5, D_{10}, D_{20}, D_{35}$ ) is well represented by the PSO model. This is revealed by the high  $R^2$  values ( $R^2 = 0.99$ ). Capping nano-ferrite with dextrose frequently changes the adsorption kinetics, from simple surface-limited physisorption to more sophisticated, chemically driven adsorption processes. The modified surface chemistry of capped  $\text{Ni}_{0.6}\text{Zn}_{0.2}\text{Sb}_{0.2}\text{FD}$  adsorbs the MV molecules through strong interactions such as surface complexation, covalent bond formation, and electron sharing with MV molecules.<sup>54</sup> Furthermore, a close similarity was observed between  $q_{\text{exp}}$  and  $q_{\text{cal}}$ . Additionally, according to the Elovich model, the rate of adsorption  $\alpha$  for MV was significantly higher than the



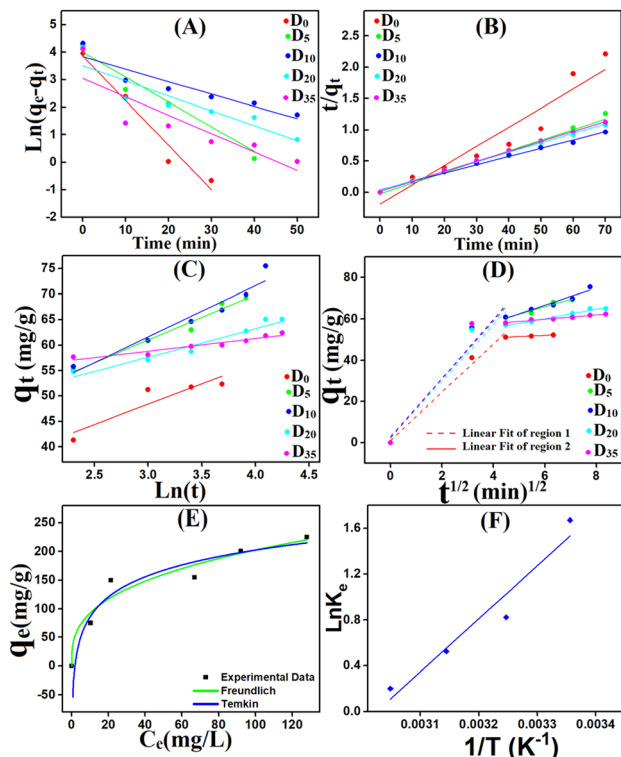


Fig. 13 The linear relationships derived from: (a) pseudo-first-order kinetic plots, (b) pseudo-second-order kinetic plots, (c) the Elovich model, (d) the IPD model,  $D_0$ ,  $D_5$ ,  $D_{10}$ ,  $D_{20}$ ,  $D_{35}$  are dextrose concentration in  $\text{Ni}_{0.6}\text{Zn}_{0.2}\text{Sb}_{0.2}\text{FD}$ . and (e) fitting representations of non-linear isotherm models for the adsorption of MV on  $\text{Ni}_{0.6}\text{Zn}_{0.2}\text{Sb}_{0.2}\text{FD}_{10}$ , and (f) van't Hoff's plot for the adsorption of MV onto  $\text{Ni}_{0.6}\text{Zn}_{0.2}\text{Sb}_{0.2}\text{FD}_{10}$ .

rate of desorption  $\beta$ , supporting the reliability of the pseudo-second-order kinetic model.<sup>55</sup> As shown in Fig. 13(d), two linear regions exist in all samples, indicating the presence of multiple stages in the adsorption process. Table 3 shows that the  $k_i$  values of region one are greater than those of region two. The first region indicates the rapid diffusion stage with external surface adsorption of MV dye, while the second region reveals a slow adsorption stage associated with the intraparticle diffusion of MV within the pores of the adsorbents. Moreover, the non-zero values of  $C$  indicate that the intra-particle diffusion is not the only rate-determining step.

### 3.8. Adsorption isotherm

Adsorption isotherm models play a fundamental role in describing the interactive behavior between the adsorbate and adsorbent. They are crucial for investigating the mechanisms of adsorption, the properties of the surface, and the affinity of the adsorbent.<sup>56</sup> The non-linear isotherm models, including the Freundlich and Temkin, were employed. Their detailed descriptions are provided in the supplementary data (Text S1). The non-linear fit of these models for the adsorption of MV on  $\text{Ni}_{0.6}\text{Zn}_{0.2}\text{Sb}_{0.2}\text{FD}_{10}$  is presented in Fig. 13(e). Also, the parameters obtained from the non-linear isotherm models are presented in Table 4. The adsorption behavior is best fit to the Temkin non-linear isotherm of correlation,  $R^2 = 0.94$ . This fitting indicates that the adsorption process is dependent on the heat of adsorption ( $b_T$ ). When the  $b_T$  is a positive value, the adsorption process is exothermic. It is known from Temkin behavior that chemisorption often has typical adsorption

energies,  $\frac{RT}{b_T} \ln(K_T)$ , ranging from 8–16  $\text{kJ mol}^{-1}$ , while

Table 3 The derived kinetic parameters of the methyl violet adsorption onto  $\text{Ni}_{0.6}\text{Zn}_{0.2}\text{Sb}_{0.2}\text{FD}$

Kinetic models and parameters	$D_0$	$D_5$	$D_{10}$	$D_{20}$	$D_{35}$
Experimental, $q_{\text{exp}}$ ( $\text{mg g}^{-1}$ )	31.60	57.80	75.50	65.10	61.90
<b>Pseudo 1st order</b>					
$R^2$	0.95	0.90	0.84	0.79	0.70
Calculated, $q_{\text{cal}}$ ( $\text{mg g}^{-1}$ )	47.60	54.65	46.22	33.49	21.29
$k_1$	0.162	0.090	0.045	0.055	0.067
<b>Pseudo 2nd order</b>					
$R^2$	0.90	0.97	0.99	0.99	0.99
Calculated, $q_{\text{cal}}$ ( $\text{mg g}^{-1}$ )	32.52	58.31	75.41	66.05	62.58
$k_2$	-0.005	-0.011	0.004	0.007	0.017
<b>Elovich</b>					
$\alpha$ ( $\text{mg g}^{-1} \text{min}^{-1}$ )	170.99	432.58	231.92	8480.82	$2.4 \times 10^9$
$\beta$ ( $\text{g mg}^{-1}$ )	0.13	0.11	0.10	0.18	0.40
$R^2$	0.76	0.96	0.92	0.91	0.90
<b>IPD</b>					
Region 1					
$C$ ( $\text{mg g}^{-1}$ )	0.94	2.25	2.35	2.66	3.07
$k_i$ ( $\text{mg g}^{-1} \text{min}^{0.5}$ )	11.76	14.33	14.38	13.62	13.97
$R^2$	0.98	0.92	0.91	0.88	0.84
Region 2					
$C$ ( $\text{mg g}^{-1}$ )	48.76	44.81	41.73	46.56	53.56
$k_i$ ( $\text{mg g}^{-1} \text{min}^{0.5}$ )	0.56	3.52	4.16	2.27	1.06
$R^2$	0.99	0.92	0.94	0.95	0.97



**Table 4** The parameters derived from the non-linear isotherm models for methyl violet adsorption onto Ni<sub>0.6</sub>Zn<sub>0.2</sub>Sb<sub>0.2</sub>FD<sub>10</sub>

Isotherm models and parameters	Value
<b>Freundlich</b>	
$K_F$	42.192
$n$	2.936
$\frac{1}{n}$	0.341
$R^2$	0.937
<b>Temkin</b>	
$b_T$ (J mol <sup>-1</sup> )	48.827
$K_T$ (L mg <sup>-1</sup> )	0.540
$\frac{RT}{b_T} \ln(K_T)$	-31.27
$R^2$	0.940

physisorption has typical energies less than -40 kJ mol<sup>-1</sup>.<sup>57</sup> Herein, the typical adsorption energy of MV on Ni<sub>0.6</sub>Zn<sub>0.2</sub>Sb<sub>0.2</sub>FD<sub>10</sub>,  $\frac{RT}{b_T} \ln(K_T) = -31.27$  kJ mol<sup>-1</sup>, besides,  $b_T$  value is less than 80 kJ mol<sup>-1</sup> (ref. 57) which confirms the physisorption interaction. Moreover, the Freundlich model provides a good explanation for adsorption behavior, owing to adjusted  $R^2 = 0.937$ . Since  $n > 1$ , the adsorption is favorable and occurs in terms of physical behavior. The heterogeneity factor ( $\frac{1}{n}$ ) < 1, which provides high surface heterogeneity. The higher value of  $K_f$  reflects the greater adsorption potential.

### 3.9. Thermodynamic study

Thermodynamic parameters were analyzed to understand the mechanisms, spontaneity, energetics, and feasibility of MV adsorption processes during the temperature range 25–55 °C. The van't Hoff formula was applied to calculate Gibbs' free energy change ( $\Delta G$ ), enthalpy change ( $\Delta H$ ), and entropy change ( $\Delta S$ ), eqn (24)–(26).<sup>58–61</sup>

$$\ln K_e = \frac{\Delta S}{R} - \frac{\Delta H}{RT}, \quad (24)$$

$$\Delta G = \Delta H - T\Delta S, \quad (25)$$

$$K_e = \frac{q_e}{C_e}, \quad (26)$$

where  $K_e$  is the equilibrium constant,  $q_e$  is the amount of adsorbed MV per gram of the adsorbent at equilibrium (mg g<sup>-1</sup>),  $C_e$  is the concentration of MV at equilibrium,  $R$  is the ideal gas constant, and  $T$  is the temperature, the van't Hoff plot was depicted in Fig. 13(f).

The  $\Delta G$  values for the adsorption process of MV onto Ni<sub>0.6</sub>Zn<sub>0.2</sub>Sb<sub>0.2</sub>FD<sub>10</sub> at different temperatures were negative, -3.79, -2.63, -1.46, and -0.30 kJ mol<sup>-1</sup> for 25, 35, 45, and 55 °C, suggesting that adsorption occurred feasibly and spontaneously.  $\Delta H$  value (-38.5 kJ mol<sup>-1</sup>) suggests that the adsorption process of MV onto Ni<sub>0.6</sub>Zn<sub>0.2</sub>Sb<sub>0.2</sub>FD<sub>10</sub> is exothermic. It is

known that the  $\Delta H$  parameter may be used to categorize adsorption as physical when  $\Delta H < 84$  kJ mol<sup>-1</sup>, or chemical when  $184 < \Delta H < 420$  kJ mol<sup>-1</sup>.<sup>41</sup> In our study, the  $\Delta H$  value indicates that MV adsorption is a physical process, consistent with the  $\Delta G$  parameter values, Fig. 13(f). Additionally, the negative entropy change  $\Delta S^\circ$  (-116.47 J mol<sup>-1</sup> K<sup>-1</sup>) is evidence of a reduction in collision randomness between MV molecules and Ni<sub>0.6</sub>Zn<sub>0.2</sub>Sb<sub>0.2</sub>FD<sub>10</sub> interface.<sup>42</sup>

### 3.10. The plausible MV elimination mechanism

To clarify the mechanism of MV adsorption on Ni<sub>0.6</sub>Zn<sub>0.2</sub>Sb<sub>0.2</sub>FD<sub>10</sub>, FTIR was analyzed before and after MV adsorption. According to Fig. 14, the metal-oxygen (M-O) stretching vibrations of tetrahedral (A) sites were shown at the band with strong absorption and a greater wavenumber at 587 cm<sup>-1</sup>, while the M-O octahedral (B) site vibrations in Ni<sub>0.6</sub>Zn<sub>0.2</sub>Sb<sub>0.2</sub>FD<sub>10</sub> were depicted at the reduced intensity absorbance band with a lower wavenumber at 400 cm<sup>-1</sup>. As a result of these M-O spectra, the spinel structure has been confirmed.<sup>20</sup> The signature bands of OH, aliphatic asymmetric C-H, C=O, and C-C were recorded at 3400 cm<sup>-1</sup>, 2915 cm<sup>-1</sup>, 1655 cm<sup>-1</sup>, and 1473 cm<sup>-1</sup> stretching frequencies. While the bending character vibration of C-H appeared at 1361 cm<sup>-1</sup>.<sup>62</sup> The observed band at 2360 cm<sup>-1</sup> is attributed to CO<sub>2</sub> present in the atmosphere. Using the Ni<sub>0.6</sub>Zn<sub>0.2</sub>Sb<sub>0.2</sub>FD<sub>10</sub> to adsorb cationic MV dye caused a dramatic shift in the position and intensity of the spectrum's peaks, Fig. 14. The bands of O-H, C=O, and C-C apparently shifted from 3400 cm<sup>-1</sup>, 1655 cm<sup>-1</sup>, and 1473 cm<sup>-1</sup> to 3393 cm<sup>-1</sup>, 1635 cm<sup>-1</sup>, and 1458 cm<sup>-1</sup> before and after loading MV, respectively. Besides, the stretching and bending vibrations of C-H migrated from 2915 cm<sup>-1</sup> and 1361 cm<sup>-1</sup> to 2926 cm<sup>-1</sup> and 1368 cm<sup>-1</sup>, respectively. Furthermore, metal-oxo bond shifting from 587 cm<sup>-1</sup> and 400 cm<sup>-1</sup> to 594 cm<sup>-1</sup> and 416 cm<sup>-1</sup> occurred, respectively. The additional stretching vibration band appeared at 1164 cm<sup>-1</sup>, corresponding to C-N in MV. The absence of the 2360 cm<sup>-1</sup> band indicated that CO<sub>2</sub> was poorly adsorbed, and MV physically removed or inhibited it from

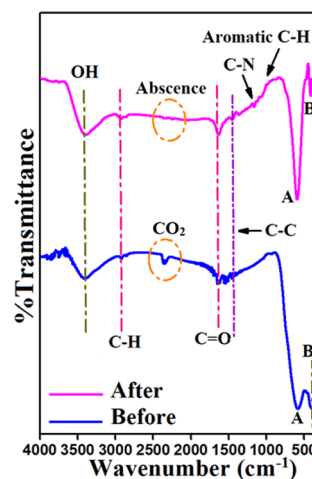


**Fig. 14** FTIR before and after MV adsorption on Ni<sub>0.6</sub>Zn<sub>0.2</sub>Sb<sub>0.2</sub>FD<sub>10</sub> surface.



**Table 5** The excellent adsorption efficiency of MV on  $\text{Ni}_{0.6}\text{Zn}_{0.2}\text{Sb}_{0.2}\text{FD}_{10}$  with a fast equilibrium period in comparison with other capped and non-capped ferrites

Adsorbent	$q_{\text{max}}$ ( $\text{mg g}^{-1}$ )	Experimental conditions (adsorbent amount, pH, dye concentration, contact time)	References
MMT/GO/CoFe <sub>2</sub> O <sub>4</sub>	97.26	1 g L <sup>-1</sup> , 8, 10 mg L <sup>-1</sup> , 40 min	42
Nickel ferrite	380	25 mg, 11, 10 mg L <sup>-1</sup>	47
AC/CoFe <sub>2</sub> O <sub>4</sub>	83.90	3 g L <sup>-1</sup> , 8, 10 mg L <sup>-1</sup> , 40 min	63
NiFe <sub>2</sub> O <sub>4</sub> -SDS	5.195	0.1 g, 5.5, 15 mg L <sup>-1</sup> , 25 min	64
Ni <sub>0.5</sub> Zn <sub>0.5</sub> Fe <sub>2</sub> O <sub>4</sub> nanocomposite	500	0.06 g, 7, 20 mg L <sup>-1</sup> , 120 min	65
NiCuZnFe <sub>2</sub> O <sub>4</sub> ferrite-biochar composite	325.5	30 mg, 8, 250 mg L <sup>-1</sup> , 120 min	66
SDS-coated GS nanoparticles	174.2	10 mg, 3, 15 mg L <sup>-1</sup> , 5 min	67
Ni <sub>0.6</sub> Zn <sub>0.2</sub> Sb <sub>0.2</sub> FD <sub>10</sub>	75.5	20 mg, 7, 10 ppm, 60 min	This study

adhering around. Multiple out-of-plane C–H bending vibration peaks were found between 600 and 1000  $\text{cm}^{-1}$ , indicating an aromatic structure.<sup>47</sup> In conclusion, there is a hybrid adsorption mechanism that is defined by the concurrent presence of both chemisorption and physisorption processes. This is consistently supported by evidence from the spectroscopic (FT-IR) shifts, the fitted kinetic and isotherm models, and the estimated thermodynamic parameters. MV elimination on  $\text{Ni}_{0.6}\text{Zn}_{0.2}\text{Sb}_{0.2}\text{FD}_{10}$  surfaces could be attributed to physical pathways, including coordination, hydrogen bonding, van der Waals forces, and hydrophobic electrostatic contact. This elimination route occurred through interaction between M–O, –OH, C=O, C–C, and C–O binding sites on the  $\text{Ni}_{0.6}\text{Zn}_{0.2}\text{Sb}_{0.2}\text{FD}_{10}$  adsorbent with nitrogen, and aromatic rings on the MV molecule's surface. The FTIR analysis following MV adsorption supported this conclusion. Additionally, the isotherms of MV adsorption onto  $\text{Ni}_{0.6}\text{Zn}_{0.2}\text{Sb}_{0.2}\text{FD}_{10}$  surfaces also demonstrate physical behavior of these adsorption processes. Temkin's isotherm model is the best for describing the physisorption mechanism as  $b_t < 80 \text{ kJ mol}^{-1}$ . It suggests that this sort of adsorption includes weak van der Waals forces, resulting in the creation of multilayers on the  $\text{Ni}_{0.6}\text{Zn}_{0.2}\text{Sb}_{0.2}\text{FD}_{10}$  surface.<sup>48</sup> This was aligned with the thermodynamic  $\Delta H$  value ( $-38.5 \text{ kJ mol}^{-1}$ ) that proved the physisorption.<sup>41</sup> Whereas, the most suitable kinetic model for MV adsorption on capped  $\text{Ni}_{0.6}\text{Zn}_{0.2}\text{Sb}_{0.2}\text{FD}_{10}$  was pseudo-second order. Since dextrose capping of  $\text{Ni}_{0.6}\text{Zn}_{0.2}\text{Sb}_{0.2}\text{F}$  alters the surface chemistry of the nano-ferrite adsorbent. This change is responsible for the chemisorption MV removal on  $\text{Ni}_{0.6}\text{Zn}_{0.2}\text{Sb}_{0.2}\text{FD}_{10}$  surface. This was confirmed by the Elovich model, which computed parameters  $\alpha$  and  $\beta$  as the adsorption rate is higher than the desorption rate ( $\alpha > \beta$ ).<sup>55</sup>

### 3.11. Comparative study

Table 5 shows that  $\text{Ni}_{0.6}\text{Zn}_{0.2}\text{Sb}_{0.2}\text{FD}_{10}$  has a strong affinity for MV molecules with excellent adsorption efficiency in a short equilibrium time in comparison with other adsorbents.  $\text{Ni}_{0.6}\text{Zn}_{0.2}\text{Sb}_{0.2}\text{FD}_{10}$  attained high adsorption capability in neutral circumstances (pH = 7) and prevented solution neutralization after adsorption. The prior studies required a mildly acidic or weak and strong basic media to achieve a considerable removal efficiency.<sup>42,47,63–67</sup> Furthermore,  $\text{Ni}_{0.6}\text{Zn}_{0.2}\text{Sb}_{0.2}\text{FD}_{10}$  reached high removal percent and adsorption capacity by 78.5% and

75.5  $\text{mg g}^{-1}$ , respectively, for 10 ppm MV, neutral pH, 20 mg adsorbent dosage in equilibrium time = 60 min. This significant MV removal of  $\text{Ni}_{0.6}\text{Zn}_{0.2}\text{Sb}_{0.2}\text{FD}_{10}$  is higher than previously fabricated adsorbents, as depicted in Table 5.

## 4. Conclusion

Different concentrations of dextrose monohydrate were utilized to cap  $\text{Ni}_{0.6}\text{Zn}_{0.2}\text{Sb}_{0.2}\text{Fe}_2\text{O}_4$ . Several optical parameters were calculated, and the effect of capping agent concentration was studied. It was found that  $\text{Ni}_{0.6}\text{Zn}_{0.2}\text{Sb}_{0.2}\text{FD}_{10}$  had the highest transmittance, making it suitable for optoelectronic applications. The band gap energy varied between 2.71 and 3.05 eV, where  $\text{Ni}_{0.6}\text{Zn}_{0.2}\text{Sb}_{0.2}\text{FD}_5$  sample registered the lowest value, while  $\text{Ni}_{0.6}\text{Zn}_{0.2}\text{Sb}_{0.2}\text{FD}_{35}$  attained the highest value. The refractive index value ranged between 2.21 and 2.39 for all samples. Moreover, the PL studies shed light on the potential use of the synthesized nanoferrites in blue-chip light-emitting diode, by studying their chromaticity diagram. Moreover, the adsorption activity of the  $\text{Ni}_{0.6}\text{Zn}_{0.2}\text{Sb}_{0.2}\text{FD}_{10}$  against MV was examined. It showed the best performance with a removal efficiency of 78.5% at pH = 7, 60 min for 10 ppm MV by 10 mg  $\text{Ni}_{0.6}\text{Zn}_{0.2}\text{Sb}_{0.2}\text{FD}_{10}$ . The maximum adsorption capacity reached 75.5  $\text{mg g}^{-1}$  at equilibrium time. Moreover,  $\text{Ni}_{0.6}\text{Zn}_{0.2}\text{Sb}_{0.2}\text{FD}_{10}$  was stable and reusable for up to five cycles. MV adsorption efficiency is substantially improved by the synergistic combination of two removal pathways. The first one is a physical route including coordination, hydrogen bonding, van der Waals forces, hydrophobic electrostatic contact, and/or pore filling. While the second route is chemical, involving covalent and hydrogen bonding. The MV adsorption study on  $\text{Ni}_{0.6}\text{Zn}_{0.2}\text{Sb}_{0.2}\text{FD}_{10}$  matches well with pseudo-second-order and follows the Temkin non-linear isotherm model. Furthermore, MV Adsorption occurred spontaneously and exothermically at temperatures ranging from 25 to 55 °C.

## Author contributions

All the authors contributed to this study. Nourhan Mohamed Gaber: adsorption studies performance, data collection, data curation, data analysis, formal analysis, and writing. Leen W. El Khatib: sample preparation, data collection, data curation, data analysis, formal analysis, and writing. Amani Aridi: review and



editing. Alaa M. Abdallah: data curation, formal analysis, and review and editing. Gehan M. El-Subruiti: conceptualization, review and supervision. Mirna Omar: adsorption studies performance, data collection, data analysis, and writing. Sarah Omar: adsorption studies performance, data collection, data analysis, and writing. Ramadan Awad: conceptualization, review and supervision. All authors reviewed and approved the manuscript.

## Conflicts of interest

The authors declare that they have no competing interests relevant to this article's content.

## Data availability

The datasets supporting the findings of this study are available within the article and its supplementary information (SI) files.

Supplementary information (SI) is available. See DOI: <https://doi.org/10.1039/d5ra08391e>.

## Acknowledgements

The authors declare that no funds, grants, or other support were received during the preparation of this manuscript.

## References

- 1 A. Akbari, H. Abbasi, M. Shafiee and H. Baniyasi, *Int. J. Biol. Macromol.*, 2024, **265**, 130750.
- 2 A. N. M. Faizal, N. R. Putra and M. A. A. Zaini, *Part. Sci. Technol.*, 2023, **41**, 730–739.
- 3 L. R. Bonetto, F. Ferrarini, C. de Marco, J. S. Crespo, R. Guégan and M. Giovanela, *J. Water Process Eng.*, 2015, **6**, 11–20.
- 4 A. N. Mohd Faizal, N. R. Putra, A. H. Abdul Aziz, A. Agi and M. A. Ahmad Zaini, *J. Clean. Prod.*, 2024, **447**, 141637.
- 5 M. Sadiku, T. Selimi, A. Berisha, A. Maloku, V. Mehmeti, V. Thaçi and N. Hasani, *Toxics*, 2022, **10**, 445.
- 6 Y. S. Al-Degs, M. I. El-Barghouthi, A. H. El-Sheikh and G. M. Walker, *Dyes Pigments*, 2008, **77**, 16–23.
- 7 Z.-X. Gong, M. Steven, Y.-T. Chen, L.-Z. Huo, H. Xu, C.-F. Guo, X.-J. Yang, Y.-X. Wang and X.-P. Luo, *RSC Adv.*, 2024, **14**, 25619–25628.
- 8 N. M. Gaber, G. M. El-Subruiti, A. M. Omer and A. S. Eltaweil, *Surf. Interfaces*, 2024, **51**, 104528.
- 9 A. Soufi, H. Hajjaoui, R. Elmoubarki, M. Abdennouri, S. Qourzal and N. Barka, *Appl. Surf. Sci. Adv.*, 2021, **6**, 100145.
- 10 R. Javed, A. Sajjad, S. Naz, H. Sajjad and Q. Ao, *Int. J. Mol. Sci.*, 2022, **23**, 10521.
- 11 A. K. Sidhu, N. Verma and P. Kaushal, *Front. Nanotechnol.*, 2022, **3**, 801620.
- 12 L. W. E. Khatib, A. M. Abdallah, M. Noun, N. E. Ghouch, G. O. Younes and R. Awad, *J. Mater. Sci. Mater. Electron.*, 2025, **36**, 700.
- 13 R. Javed, M. Zia, S. Naz, S. O. Aisida, N. ul Ain and Q. Ao, *J. Nanobiotechnology*, 2020, **18**, 172.
- 14 T. Prabhakaran, R. V. Mangalaraja, J. C. Denardin and K. Varaprasad, *J. Mater. Sci. Mater. Electron.*, 2018, **29**, 11774–11782.
- 15 R. Javed, M. Usman, S. Tabassum and M. Zia, *Appl. Surf. Sci.*, 2016, **386**, 319–326.
- 16 H. M. Kamari, M. G. Naseri and E. B. Saion, *Metals*, 2014, **4**, 118–129.
- 17 M. Goodarz Naseri, E. Saion and N. Khalil Zadeh, *Int. Nano Lett.*, 2013, **3**, 19.
- 18 J. I. Goldstein, D. E. Newbury, J. R. Michael, N. W. M. Ritchie, J. H. J. Scott and D. C. Joy, *Scanning Electron Microscopy and X-Ray Microanalysis*, Springer, 2017.
- 19 J. F. Watts and J. Wolstenholme, *An Introduction to Surface Analysis by XPS and AES*, John Wiley & Sons, 2019.
- 20 R. Yassine, A. M. Abdallah, R. S. Hassan, N. Yaacoub, R. Awad and Z. Bitar, *J. Nanoparticle Res.*, 2023, **25**, 90.
- 21 A. M. Abdallah and R. Awad, *Phys. B Condens. Matter*, 2022, **629**, 413651.
- 22 C. Kumari, H. K. Dubey, F. Naaz and P. Lahiri, *Phase Transit.*, 2020, **93**, 207–216.
- 23 R. Talebi, M. Nasiri and S. Rahnamaeiyan, *J. Mater. Sci. Mater. Electron.*, 2016, **27**, 1500–1506.
- 24 W. Chehade, H. Basma, A. M. Abdallah, R. Sayed Hassan and R. Awad, *Ceram. Int.*, 2022, **48**, 1238–1255.
- 25 A. Al-Hammadi and S. Khoreem, *Biointerface Res. Appl. Chem.*, 2023, **13**, 168.
- 26 A. Sagar, S. Bhardwaj, A. Gupta, H. Tripathi and R. Shukla, *Interactions*, 2024, **245**, 86.
- 27 S. J. Salih and W. M. Mahmood, *Heliyon*, 2023, **9**, e16601.
- 28 S. Noreen and A. Hussain, *Opt. Mater.*, 2023, **139**, 113797.
- 29 M. Chebbi, S. Mansouri, S. Hcini, I. Ghiloufi, A. Mimouni and L. E. Mir, *J. Mol. Struct.*, 2024, **1295**, 136740.
- 30 A. Hashim, *J. Inorg. Organomet. Polym. Mater.*, 2021, **31**, 2483–2491.
- 31 T. S. Soliman and S. A. Vshivkov, *J. Non-Cryst. Solids*, 2019, **519**, 119452.
- 32 C. S. Pawar, M. P. Gujar and V. L. Mathe, *J. Supercond. Nov. Magn.*, 2017, **30**, 615–625.
- 33 H. Lemziouka, A. Boutahar, R. Moubah, L. H. Omari, S. Bahhar, M. Abid and H. Lassri, *Vacuum*, 2020, **182**, 109780.
- 34 V. L. Savithri Vatsalya, G. S. Sundari, Ch. S. L. N. Sridhar, I. L. Prasanna and Ch. S. Lakshmi, *J. Lumin.*, 2022, **252**, 119314.
- 35 E. M. Assim, *J. Alloys Compd.*, 2008, **463**, 55–61.
- 36 R. Sharma, P. Thakur, M. Kumar, P. B. Barman, P. Sharma and V. Sharma, *Ceram. Int.*, 2017, **43**, 13661–13669.
- 37 A. M. Abdallah, M. Noun and R. Awad, *Appl. Phys. A*, 2021, **127**, 760.
- 38 S. Debnath and R. Das, *J. Mol. Struct.*, 2020, **1199**, 127044.
- 39 M. A. Osman and A. G. Abd-Elrahim, *Opt. Mater.*, 2018, **77**, 1–12.
- 40 A. Ivanets, V. Prozorovich, M. Roshchina, T. Kouznetsova, N. Budeiko, L. Kulbitskaya, A. Hosseini-Bandegharai, V. Masindi and V. Pankov, *Chem.–Eng. J.*, 2021, **411**, 128523.
- 41 R. Foroutan, R. Mohammadi, A. Ahmadi, G. Bikhbar, F. Babaei and B. Ramavandi, *Chemosphere*, 2022, **286**, 131632.



- 42 R. Foroutan, R. Mohammadi, F. MousaKhanloo, S. Sahebi, B. Ramavandi, P. S. Kumar and K. H. Vardhan, *Adv. Powder Technol.*, 2020, **31**, 3993–4004.
- 43 E. F. J. Duynstee and E. Grunwald, *J. Am. Chem. Soc.*, 1959, **81**, 4542–4548.
- 44 A. S. Eltaweil, N. Mohamed Gaber, G. M. El-Subruiti and A. M. Omer, *J. Mol. Liq.*, 2024, **394**, 123716.
- 45 A. Ahmadi, R. Foroutan, H. Esmaeili, S. J. Peighambardoust, S. Hemmati and B. Ramavandi, *Mater. Chem. Phys.*, 2022, **284**, 126088.
- 46 C. Li, Y. Dong, J. Yang, Y. Li and C. Huang, *J. Mol. Liq.*, 2014, **196**, 348–356.
- 47 S. Debnath and R. Das, *Ceram. Int.*, 2023, **49**, 16199–16215.
- 48 S. V. Gupta, V. V. Kulkarni and Md. Ahmaruzzaman, *Colloids Surf. Physicochem. Eng. Asp.*, 2024, **680**, 132611.
- 49 N. Hassan, A. Shahat, A. El-Didamony, M. G. El-Desouky and A. A. El-Bindary, *J. Mol. Struct.*, 2020, **1210**, 128029.
- 50 A. Almahri, K. S. Abou-Melha, H. A. Katouah, A. M. Albonayan, F. A. Saad, M. G. El-Desouky and A. A. El-Bindary, *J. Mol. Struct.*, 2023, **1293**, 136238.
- 51 M. Adel, M. A. Ahmed and A. A. Mohamed, *Environ. Nanotechnol. Monit. Manag.*, 2021, **16**, 100550.
- 52 E. M. Abd El-Monaem, M. Hosny and A. S. Eltaweil, *Chem. Eng. Sci.*, 2024, **287**, 119707.
- 53 A. M. Omer, M. El-Sayed, E. M. Abd El-Monaem, G. M. El-Subruiti and A. S. Eltaweil, *Int. J. Biol. Macromol.*, 2023, **253**, 127437.
- 54 A. Aridi, S. Rmeid, M. Y. El Sayed, K. Habanjar, G. M. El-Subruiti, E. M. Abdel Rahman, W. F. Khalil, R. Awad and N. M. Gaber, *Mater. Sci. Eng. B*, 2026, **323**, 118820.
- 55 A. S. Eltaweil, A. E. Awad, E. M. Abd El-Monaem, A. M. Shaker and G. M. El-Subruiti, *J. Mol. Struct.*, 2025, **1337**, 142143.
- 56 M. Açıkyıldız, A. Gürses, K. Güneş and D. Yalvaç, *Appl. Surf. Sci.*, 2015, **354**, 279–284.
- 57 D. Rahangdale and A. Kumar, *Carbohydr. Polym.*, 2018, **202**, 334–344.
- 58 S. Zghal, I. Jedidi, M. Cretin, S. Cerneaux and M. Abdelmouleh, *Materials*, 2023, **16**, 1015.
- 59 N. S. Ali, N. M. Jabbar, S. M. Alardhi, H. S. Majdi and T. M. Albayati, *Heliyon*, 2022, **8**, e10276.
- 60 A. R. Kul, A. Aldemir, S. Alkan, H. Elik and M. Çalışkan, *Environ. Res. Technol.*, 2019, **2**, 112–121.
- 61 N. F. Alharby, R. S. Almutairi and N. A. Mohamed, *Polymers*, 2021, **13**, 3659.
- 62 Y. Padwal, R. Chauhan, I. Jeet Chaudhary, D. J. Late, M. Ashokkumar and S. Gosavi, *Energy Adv.*, 2025, **4**, 281–295.
- 63 R. Foroutan, R. Mohammadi and B. Ramavandi, *Environ. Sci. Pollut. Res.*, 2019, **26**, 19523–19539.
- 64 N. Alizadeh and M. Mahjoub, *J. Nanoanalysis*, 2017, **4**, 8–19.
- 65 A. Afkhami, S. Sayari, R. Moosavi and T. Madrakian, *J. Ind. Eng. Chem.*, 2015, **21**, 920–924.
- 66 D. Mehta, P. N. Dave and V. Vijay Kumar, *RSC Adv.*, 2025, **15**, 33189–33208.
- 67 A. N. Tiwari, K. Tapadia and C. Thakur, *Water Sci. Technol.*, 2022, **86**, 625–642.

